Dipole-field interactions determine the CO2 reduction activity of 2D Fe-N-C single atom catalysts

Vijay, Sudarshan; Gauthier, Joseph A.; Heenen, Hendrik H.; Bukas, Vanessa J.; Kristoffersen, Henrik H.; Chan, Karen

Published in:
ACS Catalysis

Link to article, DOI:
10.1021/acscatal.0c01375

Publication date:
2020

Document Version
Peer reviewed version

Dipole-Field Interactions Determine the CO_2 Reduction Activity of 2D Fe-N-C Single Atom Catalysts

Sudarshan Vijay,[†] Joseph A. Gauthier,[‡,¶] Hendrik H. Heenen,[†] Vanessa J. Bukas,[†] Henrik H. Kristoffersen,[†] and Karen Chan[*,†]

†*CatTheory, Department of Physics, Technical University of Denmark, DK-2800, Kgs. Lyngby, Denmark*

‡*SUNCAT Center for Interface Science and Catalysis, Department of Chemical Engineering, Stanford University, Stanford, California 94305, United States*

¶*Current address: Chemical Sciences Division, Lawrence Berkeley National Laboratory, Berkeley, California 94720, United States*

E-mail: kchan@fysik.dtu.dk

Abstract

Iron-nitrogen-doped graphene (FeNC) has emerged as an exciting earth-abundant catalyst for electrochemical CO_2 reduction (CO_2R). However, standard theoretical approaches based on density functional theory (DFT) suggest complete poisoning of the active sites, and are unable to rationalize the experimentally observed dramatic pH dependence and Tafel slopes, which have a critical impact on the electrocatalytic activity. In this work, we overcome these challenges through a rigorous theoretical investigation of FeNC single atom catalysts using a combination of several state-of-the-art methods: hybrid functionals, continuum solvation, and potential dependent

electrochemical reaction energetics. Our model shows dipole-field interactions in CO_2 adsorption to determine the overall activity, which resolves the contentious origin of experimentally observed pH dependence and rationalizes differences in activity and Tafel slopes amongst different samples in experimental work. A critical conclusion of our study is that single-atom catalysts can be tuned for electrocatalytic activity not only through the traditionally considered binding energies, but also through the corresponding surface dipole moment of rate-determining surface intermediates. Our presented methodology paves the way for accurate mechanistic studies as well as the computational catalyst design of general single-atom catalysts.

Keywords: Electrocatalysis, FeNC, single atom catalysts, CO_2 Reduction, Dipole

Introduction

The electrochemical reduction of CO_2 is a promising approach to store the energy from intermittent renewable sources such as wind and solar in the form of valuable fuels and chemicals.[1,2] From the catalysis perspective, the primary barriers to commercialization are activity, selectivity, stability, and cost.[1,3] To date, the most active and selective transition metal catalyst for CO_2 reduction (CO_2R) to CO is Au, which shows current densities up to 10 mA/cm^2 at -0.4V vs. Reversible Hydrogen Electrode (RHE) with nearly 100% Faradaic efficiency in two-compartment cell configurations.[4] Single-atom catalysts which consist of earth-abundant elements such as Fe, Co, and Ni doped on a support material such as graphene, have emerged as promising alternatives to Au.[5–7] Very recently, FeNC catalysts, fabricated through pyrolysis on defected graphene and characterized within a gas-diffusion electrode showed an impressive geometric current density of 100 mA/cm^2 with Faradaic efficiency toward CO greater than 90% at -0.4 V vs. RHE. This high activity was suggested to arise from tailored Fe sites with a +3 oxidation state.[8]

From the theoretical perspective, the mechanistic study of metal-Nitrogen-Carbon (M-N-C) single-atom catalysts presents several critical challenges. The graphene support is highly

defected, which gives rise to a plethora of possible active site configurations with varying coordination to N and C, with functionalization shown to be beneficial to activity[9]. Additionally, the impact of electrolyte and the charging of the electric double layer in modelling the CO_2R activity are unclear for M-N-C but have been demonstrated to be critical on transition metals in recent studies[10] helping to better understanding reaction mechanisms.[11] While computational studies of model systems such as molecular porphyrin systems have included effects such as solvation and Hubbard-U corrections[12–14], studies using extended systems of M-N-C catalysts have generally omitted solvation and were restricted to charge-neutral thermodynamic approximations, which do not consider these phenomena. Reported adsorption energies for CO on a variety of different sites range from -0.6 to -1.2 eV.[15–17] Such large negative adsorption energies suggest CO would poison the surface with negligible CO production rates, contrary to experimental findings. As a result, the active site of these materials remains a contentious issue. Furthermore, such computational models have been unable to explain why the electrolyte pH has no impact on the CO_2R activity of FeNC catalysts on an Standard Hydrogen Electrode (SHE) scale.[18] This has been suggested to be evidence of diabatic electron transfer to CO_2, or a so-called "decoupled" proton-electron transfer that cannot be treated using a standard computational hydrogen electrode approach.[18]

In this work, we overcome the aforementioned challenges through a rigorous theoretical investigation of FeNC single atom catalysts using a combination of several state-of-the-art methods: hybrid functionals, implicit electrolyte, potential dependent reaction energetics,[19] and mean-field kinetic modelling. Through combination of hybrid calculations, analysis of temperature programmed desorption (TPD) spectra as well as microkinetic modelling, we show that standard Generalized Gradient Approximation (GGA) functionals are inadequate to accurately describe the binding energies of essential intermediates. We furthermore show that reasonably accurate energetics can be obtained with GGA functionals by including a Hubbard U correction, which circumvents the need for costly hybrid-level simulations. Through explicit consideration of the interaction between the interfacial electric field with

dipolar adsorbates, we show the experimentally observed pH independence arises from a *field-dependent* CO_2 adsorption. Our results suggest double vacancy four nitrogen doped (DV4N) vacancies to be generally more active than two nitrogen doped vacancy (DV2N) site motif and the associated simulated Tafel slopes are in line with experimental observations. A critical conclusion is that single atom catalysts should be designed not only for optimal binding energies but also for their surface dipole moments. This may be achieved, for example, by doping with other p-block elements. These findings are critical from the perspective of fundamental mechanistic understanding and pave the way towards computation-guided design of general single atom catalysts.

Results and Discussion

Comparing Binding Energies of CO*

Given the aforementioned controversy surrounding the binding energies of CO^* and other intermediates, we first compare the energies of typical GGA-level simulations of CO binding on FeN_x sites against hybrid functionals. We consider both spin-polarized RPBE and HSE06 functionals, which are prototypes for GGA-DFT and hybrid-DFT, respectively. Figure 1 shows the computed binding energy of CO on possible active sites, that were identified as most stable in Ref. 20. Redhead analysis of TPD spectra[21] was also used to ascertain a plausible range of energies based on reasonable pre-factors, shown in further detail in the Supporting Information (Note 2). Since it is likely that an ensemble of active sites bind CO, we include the entire spectra (as opposed to only considering the peak) in the estimation of the experimental binding energy, which results in a 0.4eV range of estimated adsorption energies, as illustrated by the blue band.

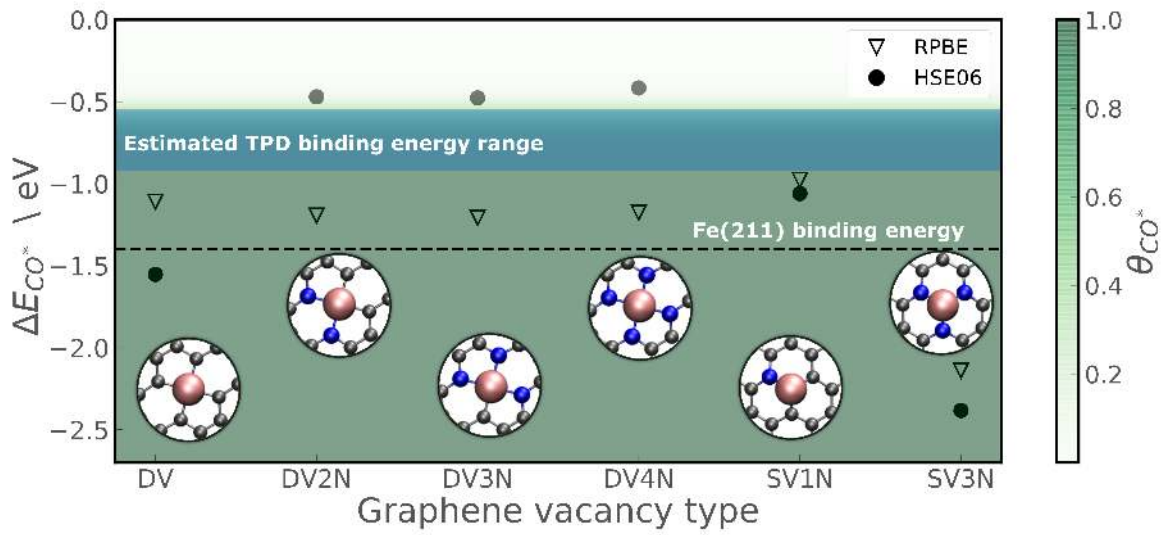

Figure 1: Comparison of adsorption energies of CO on Iron doped vacancies as proposed in Ref. 20 calculated with the GGA-RPBE functional (triangles) and the hybrid HSE06 functional (circles); Experimental estimate from TPD spectra[22] is marked by the blue band; Background fill indicates the coverage of CO predicted by the kinetic model using RPBE energetics; Fe(211) binding energies are shown with the dashed black line as a reference.

A kinetic model consisting of just thermodynamic quantities was constructed based on RPBE energetics and an assumed mechanism (see SI Note 1). Coverages of CO from this model are used to detect whether the predicted energy leads to CO poisoning the surface. In the case of RPBE, all sites considered are covered by CO. This is consistent with previous reports on these materials.[5,16] However, in the case of HSE06 results, sites corresponding to a single vacancy doped with nitrogen atoms (SV1N, SV3N) and undoped double vacancies (DV) bind CO very strongly and are expected to be poisoned under CO_2 reducing conditions. Therefore, sites that can bind CO^* weakly enough to be able to produce CO are DV2N, DV3N, DV4N (Double vacancies doped with two, three and four nitrogen atoms, respectively). Ref 20 indicates that DV2N and DV4N have formation energies of greater than -7eV with respect to graphene. Due to the noted activity and stability, we examine DV2N and DV4N as model systems in the remainder of the work. However, different experimental synthesis methods have different vacancy types on the surface. Thus, it is possible that several active sites, apart from the ones considered in this work, might contribute to

CO_2R activity. We note that there is no need for additional gas phase corrections to $CO_{(g)}$ reference used in Figure 1 as the reaction $CO_2 + H_2 \rightarrow CO + H_2O$ is well described by HSE06 (see SI Note 14). Further, the effect of using a dispersion correction is discussed in SI Note 3.

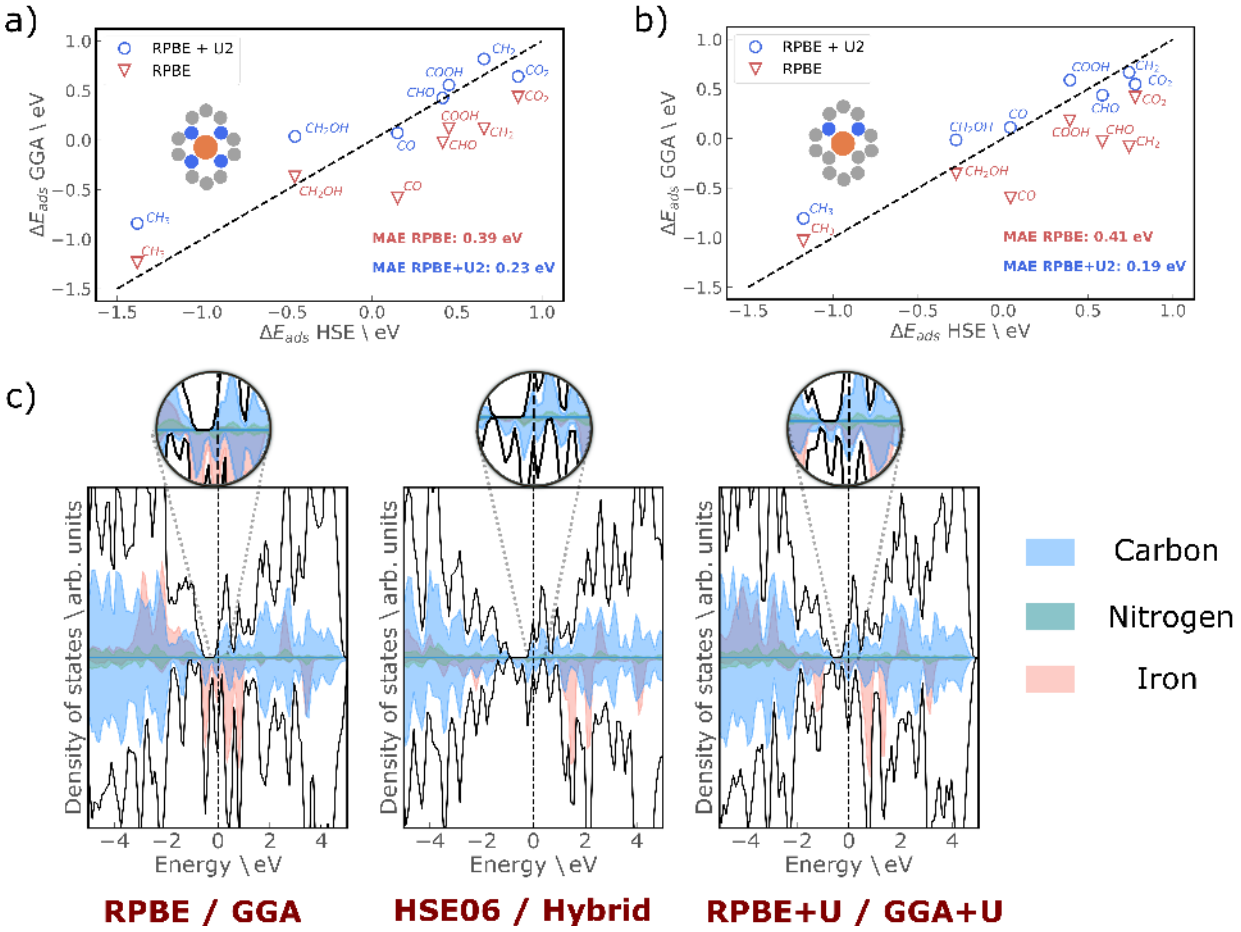

Figure 2: Comparison of RPBE and RPBE+U adsorption energies for relevant CO_2R intermediates for a) DV4N b) DV2N. Insets show the corresponding structures and mean absolute errors for both functionals. c) Projected density of states (DOS) of DV2N structure with three functionals RPBE, HSE06 and RPBE+U with U=2eV ; color scheme: Blue: Carbon, Green: Nitrogen, Orange: Iron, Black: total DOS; states near the Fermi level have been magnified for clarity; horizontal line divides spin up and spin down states.

While hybrid functional calculations provide the needed accuracy for these systems, they are prohibitively expensive for computational screening studies. We find that we can mitigate the GGA error by adding a Hubbard-U [23,24] correction to the RPBE functional, which gives

rise to essentially no additional computational cost relative to standard GGA calculations. The Hubbard-U value was varied systematically until the adsorption energies of CO on selected graphene vacancies are close to the value obtained using HSE06 (see SI Note 5). Figure 2(a,b) shows the comparison between RPBE and RPBE+U against HSE06 binding energies. Adding a Hubbard-U[23] to the *d*-states of Fe leads to a much better description of binding energies for intermediates such as CO and CH_2 for both DV2N and DV4N vacancies. mean absolute errors (MAE) as compared to HSE06 binding energies decrease from 0.4eV to 0.2eV.

Both carefully chosen Hubbard-U and HSE06 mitigate self-interaction error and open an energy gap between d-states of Fe, as illustrated in Figure 2c. In the case of RPBE, the self-interaction error leads to *d*-states at the Fermi level. The relative energy of the narrow *d*-states has implications not only for binding energies but also for determining energetics as a function of potential. In the case of DV2N and DV4N vacancies, potential dependence (dipole moments shown in SI Figure S14) is also captured by the current choice of Hubbard-U. However, we emphasize that this parameter holds only for the FeNC (see SI Note 5 for a detailed sensitivity analysis of different Hubbard-U values) and careful parameterization to experiment or higher levels of theory may be needed for other systems. Moreover, since potential dependencies can be sensitive to states around the Fermi level, HSE06 energies are used to describe potential dependent energetics.

Field-driven CO_2 adsorption

Recent experimental literature has shown that the partial current density to CO is invariant with pH on an SHE voltage scale in acidic media.[18] This effect has been associated with protons *not* being involved in the potential-limiting step, similar to other non-metallic carbon catalysts.[25,26] For this particular system, this has led to the rate limiting step being assigned as the electron transfer to CO_2:[16,18]

$$CO_2{}^* + e^- \longrightarrow CO_2{}^{*-} \quad (1)$$

Since this step does not involve proton transfer, it would satisfy the experimentally observed independence of rate on pH. However, the width of adsorbate-induced states at the Fermi level of the transition state of CO_2 adsorption on the electrode at potentials of interest precludes rate-limiting electron transfer from metal to the bent CO_2 molecule. Figure 3(b,c) shows the s,p bands of CO_2 at the transition state for CO_2 adsorbing at the DV4N, DV2N vacancy structures. As the CO_2 molecule approaches the surface, the adsorbate-induced molecular states broaden due to hybridization with the metal continuum of electronic states around the Fermi level. This broadening implies that the electron is delocalised between the bands of the metal and the CO_2 molecule. We can estimate a timescale for electron transfer (Δt) using the uncertainty relationship $\Delta E \Delta t \geq \frac{\hbar}{2}$. ΔE is given by the width of adsorbate density of states (n_a) at the Fermi level using Fermi's golden rule, which gives the rate of electron transfer as $\frac{2\pi}{\hbar} {n_a}^{27,28}$. For this system, the width is about 0.8eV (shaded in Figure 3) for both vacancies, which would correspond to a rate of $10^{15} s^{-1}$ and hence, an electron lifetime of about $10^{-15} s$. Since the motion of atoms occur on a timescale of pico-seconds, electron transfer is facile in comparison to the adsorption of CO_2.

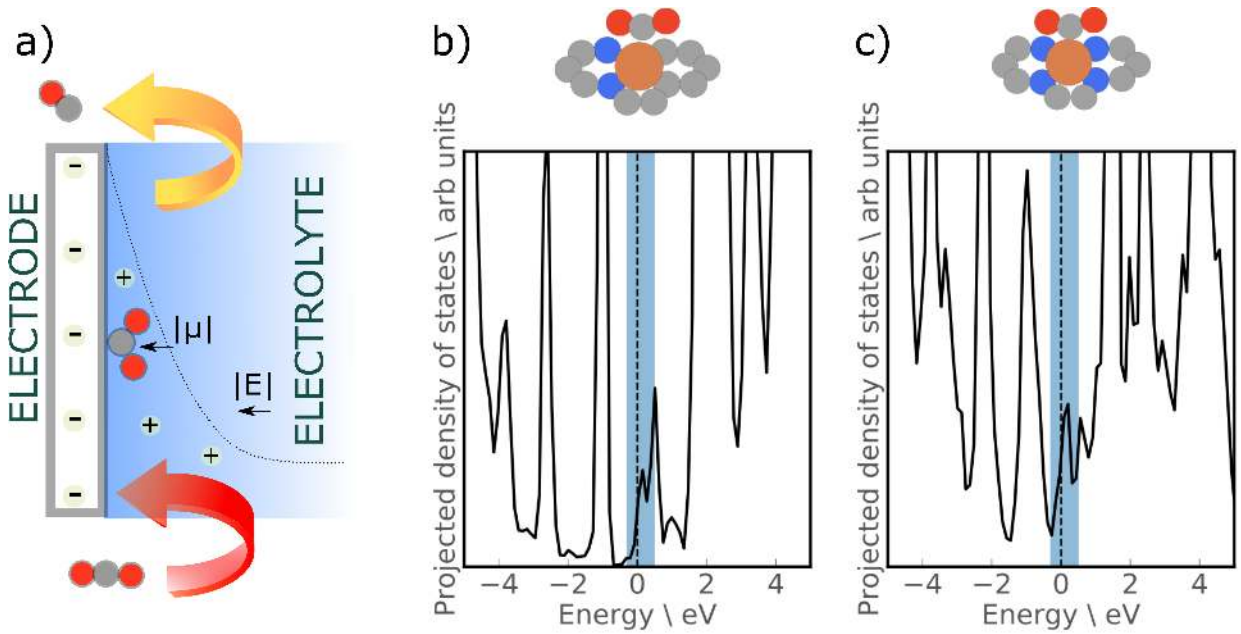

Figure 3: a) Dipole-field stabilization model of CO_2 adsorbed on FeNC electrode. the dashed line is a schematic of the electrostatic potential profile from near the electrode surface to the bulk of the solvent Density of states projected onto the s,p orbitals of CO_2 molecule at the adsorption transition state for b) DV4N c) DV2N vacancies at -0.5V vs. SHE using the HSE06 functional based on transition states obtained from RPBE+U. The DOS was obtained by varying the surface charge and converting to potential using Equation 2

Our analysis suggests that the rate-limiting step is not so much a slow electron transfer to $*CO_2^-$ but a field-stabilised CO_2 adsorption (cf. Figure 3a, showing electrostatic interaction between a dipolar, bent $*CO_2$ adsorbate and the electric field at the electrochemical interface). Since the interfacial field depends on the absolute potential, this step also shows an absolute potential dependence, i.e. the corresponding rate depends on an SHE, not RHE scale. The schematic shown in Figure 3a illustrates this by showing the dipole for bent CO_2 adsorbed on the surface and its interaction with the electrical double layer.

In the past few years, hybrid continuum/*ab initio* models of the electrochemical interface[29–32] have been developed to capture the impact of double layer charging on reaction energetics. We have recently shown the surface charge density to be the most appropriate descriptor for the electrostatic effects of the double layer on reaction energetics,[19] since it describes the variations the interfacial field *local* to the reaction site. We relate surface-charge σ dependent energetics (Figure 4(a,b) to potential-dependent ones through the interfacial capacitance C and potential of zero charge ϕ_{pzc} as follows:

$$\phi = \frac{1}{C}\sigma + \phi_{pzc} \tag{2}$$

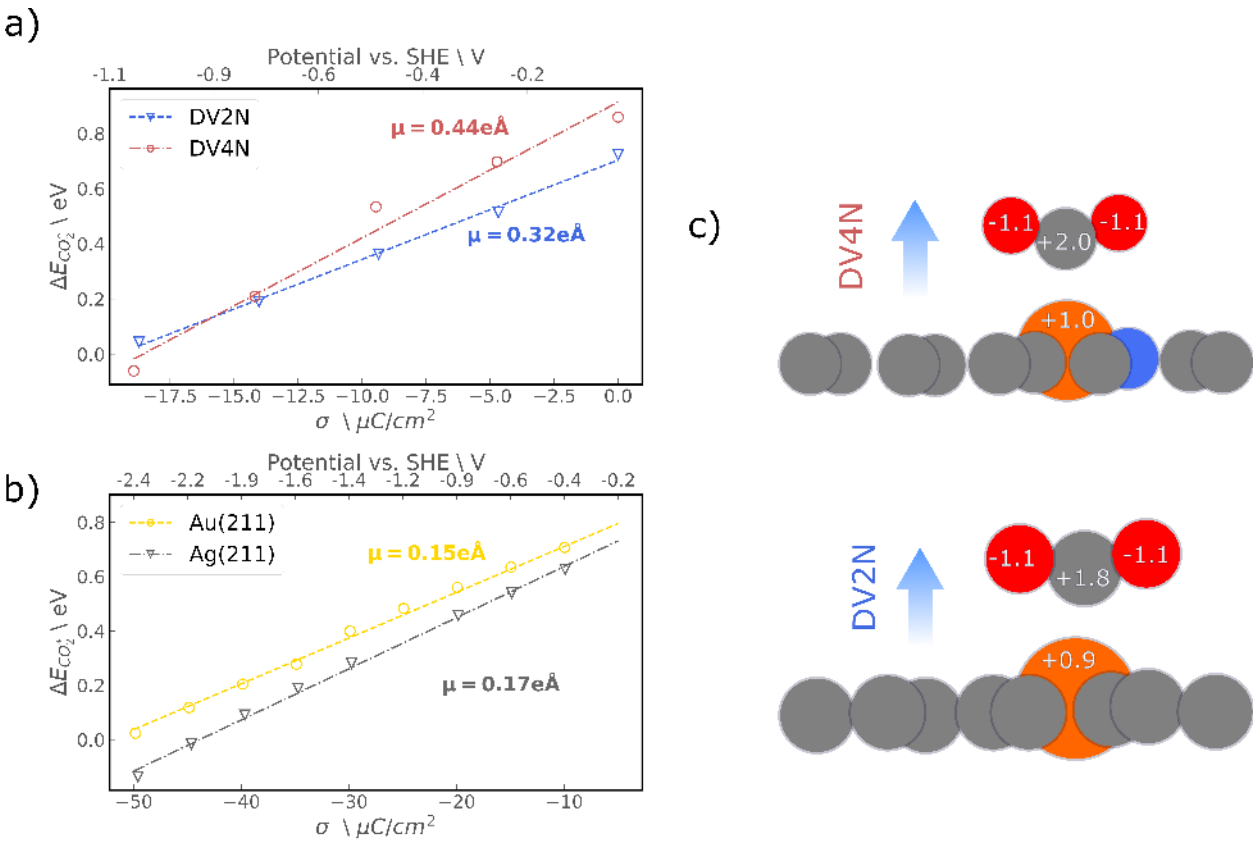

Figure 4: Change in adsorption energy of CO_2 as a function of surface charge density (σ) for a) Doped vacancies DV2N ($\Delta E = 0.036\sigma + 0.70$, with $R^2 = 0.99$) and DV4N ($\Delta E = 0.04926\sigma + 0.91$, with $R^2 = 0.97$), b) Au(211) ($\Delta E = 0.0168\sigma + 0.88$, with $R^2 = 0.99$) and Ag(211) ($\Delta E = 0.0188\sigma + 0.83$, with $R^2 = 0.99$); The surface charge is defined as the number of excess electrons per unit area. c) Calculated Bader charge for both DV4N (top) and DV2N (bottom) vacancies; Values annotated over atoms show the Bader charge; Negative values of charge densities indicate electrode reduction; points in points in a, b denote the results from DFT calculations, while lines represent the corresponding best fit lines. Any scatter of points associated with a,b arises from the change in geometry following a relaxation at each discrete surface charge.

Both quantities can, in principle, be determined from experiment.

The energy of a given adsorbate (E) is a function of its dipole moment μ and polarizability α as follows:

$$E = E_0 + \mu|\vec{\mathcal{E}}| - \frac{\alpha|\vec{\mathcal{E}}|^2}{2} \tag{3}$$

where E_0 is the energy of the zero charge state and $|\vec{\mathcal{E}}|$ is the interfacial electric field. σ and $|\vec{\mathcal{E}}|$ can be related by Gauss' law. Assuming a constant interfacial dipole, the dipole moment for a given adsorbate is given by:

$$\mu = \epsilon A \left(\Phi_0^{FS} - \Phi_0^{IS}\right) \tag{4}$$

where Φ_0^{IS} is the measured workfunction of the initial states and Φ_0^{FS} is that of the final state and A is the surface area. Figure 4 shows a linear relationship between ΔE_{CO_2} and σ. This dependence indicates that α is negligible for resonably small values of σ. We determine the dipole moment as $\epsilon_0 \frac{dE}{d\sigma}$, where ϵ_0 is the absolute permittivity and $\frac{dE}{d\sigma}$ is the slope of the lines shown in Figure 4.

For DV4N, the effect of the dipole moment of CO_2 is higher than in the case of DV2N (Figure 4a), and hence the energy drop with potential is steeper. As compared with transition metal catalysts such as gold and silver shown in Figure 4b, dipole moments of key reaction intermediates are significantly larger for these FeNC systems. While CO_2 dipoles on gold and silver step surfaces are below 0.2 eÅ, dipoles on both graphene vacancies are larger than 0.4 eÅ. A larger dipole implies a stronger stabilization from its interaction with the interfacial electric field[33] and could imply a larger symmetry factor for the reaction[34]. The impact of the dipole moment on the resulting kinetics of the CO_2R are detailed in the next section.

Micro-kinetic model

Based on field-dependent energies calculated above, we develop a mean-field micro-kinetic model to determine the potential-dependent rate of CO production from CO_2. The reaction

steps considered are

$$CO_2(g) + {}^* \longleftrightarrow {CO_2}^{TS} \longleftrightarrow {CO_2}^*$$

$${CO_2}^* + H^+ + e^- \longleftrightarrow COOH^*$$

$$COOH^* + H^+ + e^- \longleftrightarrow CO + H_2O$$

$$CO^* \longleftrightarrow CO(g)$$

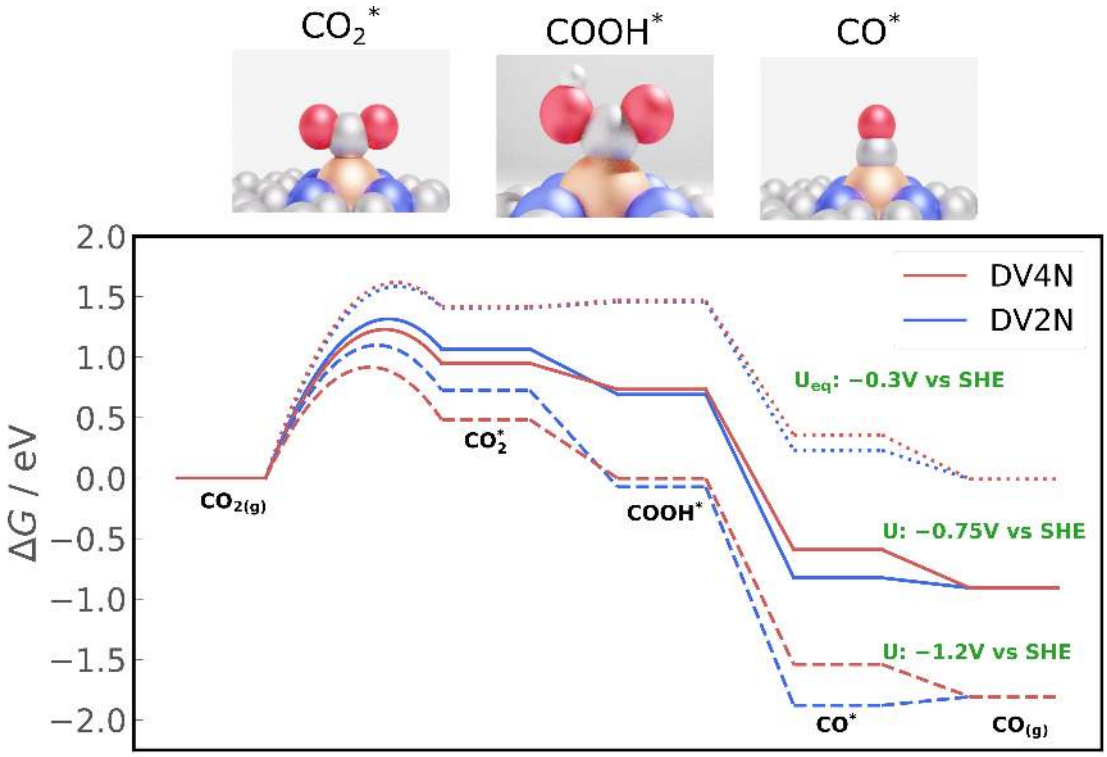

Figure 5: Free energy diagram at the theoretical equilibrium potential $U_{eq} = -0.3V$ and at two other potentials: -0.75V and -1.2V vs SHE for DV4N and DV2N vacancies at a pH of 2

pH-dependent kinetic measurements strongly suggest that proton-electron transfer is not involved in the rate limiting step.[8,18] The rate for the competing hydrogen evolution reaction (HER) shows a marked pH dependence on an SHE scale under acidic to neutral pH. This pH dependence indicates that a proton-electron transfer step limits the rate, and that hydronium

ions are active as proton donors, since H_2O as proton donors show no pH dependence.[35] In contrast to HER, CO production at the same range of pH is pH independent on an SHE scale. Thus, the rate limiting step for the CO_2R reaction does not involve a hydronium ion nor an associated proton-electron transfers.

The experimental observations are consistent with the computed free energy diagram, shown in Figure 5 on both DV4N and DV2N vacancies. The $*CO_2$ state, under relevant potentials, is the highest in energy, and the steps to the subsequent intermediates, *COOH and *CO, are all exergonic. From previous work, we found proton-electron transfers towards oxygen species to be generally facile,[36] and so we assume no additional barrier for *COOH formation. *COOH to *CO involves breaking a C−O bond, and can sometimes be rate limiting, especially at low overpotentials.[37,38] However, in this particular case, given the exergonicity of the step, even an extremely high hypothetical intrinsic barrier of 1.5eV does not make it rate limiting at the cathodic potentials considered (see SI Note 13 for further description). For the rest of this work, we therefore assume the reaction energetics are barrierless after CO_2 adsorption.

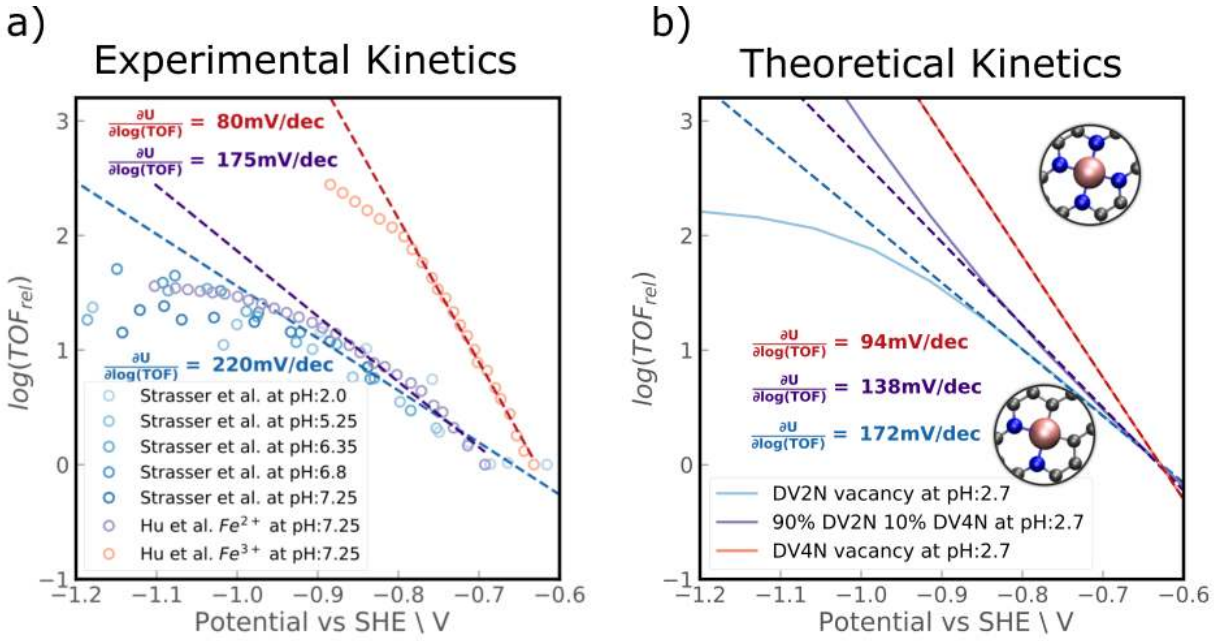

Figure 6: a) TOF taken from two publications - Strasser et al[18] and Hu et al;[8] current densities were converted to TOF by assuming all iron sites were involved in catalytic activity b) TOF obtained from mean-field microkinetic modelling; TOFs are normalized to the activity at -0.6 V vs SHE, to emphasize relative trends

Figure 6 shows a comparison of experimental[8,18] and theoretical relative turnover frequencies (TOF) (normalized to those at -0.6V vs. SHE). Experimental activity data were taken from Ref 18 and Ref 8. In the former, the activity was measured at a range of acidic pH values from 1 to 7.25, while in the latter the activity was measured at a fixed pH of 7.25 using FeNC fabricated by using either pyridinic or pyrrolic precursors. It was previously shown that the chemical identity of the N-doped vacancy can be varied based on the choice of precursor.[39] On the basis of *operando* XAS measurements, the more active catalyst was suggested to have an Fe 3^+ oxidation state and the less active one an oxidation state of Fe 2^+. The experimental TOF were calculated by assuming all Fe sites are single atom catalysts that are present on the surface and contribute to production of CO from CO_2.

Since CO_2 adsorption is the rate limiting step, the Tafel slope corresponding to activity from a given site is determined by the corresponding adsorbate dipole as follows:[38]

$$\text{Tafel slope}^{-1} = \frac{\partial \log(\text{TOF})}{\partial \Phi} = \frac{\partial \log(\text{TOF})}{\partial \Delta \text{G}_{\text{CO}_2}} \frac{d\Delta G_{\text{CO}_2}}{d\Phi} \tag{5}$$

$$= -\frac{1}{k_B T} \frac{d\Delta \text{G}_{\text{CO}_2}}{d\sigma} \frac{d\sigma}{d\Phi} = -\frac{1}{k_B T} \frac{d\Delta \text{G}_{\text{CO}_2}}{d\sigma} C \tag{6}$$

$$= \frac{1}{k_B T} \frac{C}{\epsilon} \mu \tag{7}$$

where ϵ is the permitivity of free space and $\Delta \text{G}_{\text{CO}_2}$ is the free energy of CO_2 adsorption. Where the TOF was written as $\exp\left(\frac{-\Delta \text{G}_{\text{CO}_2}}{k_b T}\right)$ Thus, the Tafel slope depends solely on the rate of change of free energy as a function of the interfacial electric field.

As previously mentioned, $CO_2{}^*$ at DV4N has a larger dipole moment as compared to that at DV2N. This is consistent with the lower Tafel slope obtained in the case of DV4N over DV2N as shown in Figure 6. Since pyrolysis is the experimental method of choice to generate these catalysts, it is not yet possible to obtain atomic precision over the active site. To show how the slope shifts when multiple sites are contributing to the activity, we show the case of 10% DV4N and 90% DV2N sites, which gives an intermediate Tafel slope.

These Tafel slopes are in line with experimentally observed ones. Hu et al.[8] observe Tafel slopes of 80 mV/dec for the more active sample and 126 mV/dec for the less active one. This difference is captured in our simple two-site model, with DV4N being significantly more active than DV2N. Strasser et al. also observe Tafel slopes of close to 200 mV / dec, which is similar to that obtained for DV2N. These results suggest that increasing the μ of active sites through e.g. the coordination environment and metal atom identity could lead to lowering of Tafel slopes and more efficient catalysts.

It is important to note that we consider here *relative*, rather than *absolute*, reaction rates due to the inherent uncertainties in quantifying TOFs from both experiment and theory. Uncertainties in the experimental determination of absolute TOFs for example lie in the assumption that all Fe atoms loaded onto the sample are catalytically active, while also presuming the same distribution of active Fe sites in samples that were prepared via differ-

ent synthesis methods.[8,18] On the other hand, theoretical DFT calculations using GGA and hybrid functionals are known to suffer from systematic errors in describing O−C−O backbone structures.[40–42] This error is believed to mainly affect the gas-phase reference leading to a constant energy offset. Ultimately, this constant energy shift yields unrealistically high reaction energies and barriers for adsorbing CO_2(g) (such as the 1 eV barrier shown in Fig. 5) and an uncertainty of 5 to 7 order of magnitude in the resulting absolute TOFs. While recent studies mitigate this issue by adding 0.30-0.45 eV corrections to gas-phase CO_2 energies,[40,41] we choose here to focus only on *relative* TOFs. This allows for circumventing the application of empirical corrections to the computed DFT energetics and our results are directly comparable to experimental data that have been normalised in the same way in Fig. 6. Most importantly, we note that all (experiment and theoretical) uncertainties in absolute TOF values do not affect the main conclusion of this study which focuses on the unique ability of single-site catalysts to tune $*CO_2$ dipoles and hence significantly change the predicted Tafel slopes (which are invariant to whether absolute or relative TOFs are considered). For reasons of completeness, we nevertheless include both absolute and relative TOF values as a function of applied potential in the SI. We also note that solvation energies are critical to accurate prediction of onset potential and reaction kinetics.[14] By referring to *relative* rather than *absolute* rates, however, we effectively cancel out any systematic errors associated with implicit solvation for a given surface species.

Another point of difference between the vacancies is that CO desorption becomes rate limiting for DV2N at large potentials, while CO_2 adsorption stays rate limiting throughout the explored potential range for DV4N. The shift in rate limiting step is shown in a degree of rate control (sensitivity) analysis,[43] coverage of CO and change in Tafel slope. A degree of rate control analysis was carried out as follows.

$$\mathrm{DRC} = \frac{d\log(\mathrm{TOF})}{dG_i} \tag{8}$$

where G_i is the free energy of each intermediate. SI Figure S8 shows that at very reducing

potentials, the rate is largely influenced by CO binding free energies. The rate would be increased by decreased CO_2 transition state energies over the whole potential range. Corresponding coverage plots for DV2N are shown in SI Figure S7. The increase in CO coverage corresponds to the change in Tafel slope seen in Figure 6.

We also consider the pathway to CH_4, which is a minor product formed on these materials. For potential ranges where coverages of CO would be very small, there would be little to no CH_4 production. However, once the coverage of CO becomes substantial, the Faradaic efficiency of CH_4 as compared to CO would increase. For a possible reaction pathway, intermediate binding energies as a function of surface charge were calculated. SI Figure S10 shows the TOF obtained from the model as well as those from Strasser et al.[18] CH_4 production in both cases are pH dependent, indicating that a proton-electron transfer step would be rate limiting for electrochemical reduction of CO to CH_4. Since these are based on thermodynamic variations in energy alone, we focus here on the qualitative pH dependence.

The above microkinetic analysis, in summary, shows the following: 1) Tafel slopes can be tuned by appropriately designing sites that induce large dipole moments in adsorbates 2) consideration of the effects of pH, potential and electric field in simulations are essential to an accurate mechanistic description of CO_2R on FeNC catalysts.

Conclusions

In this work, we presented an *ab initio* investigation of the activity of Fe-N-C catalysts for CO_2 reduction. We showed that a combination of state-of-the-art methods, hybrid functionals, implicit electrolyte and potential dependent electrochemical reaction energetics, are all required for a rigorous mechanistic analysis. We find that the rate limiting step on these materials is generally a field-driven CO_2 adsorption step, which gives rise to the dramatic pH independence that is observed experimentally. This physical explanation appears to be in accordance with the latest experimental studies. We find that the activity is highly de-

pendent on the configuration of the active site, with significant differences in the Tafel slope between DV2N and DV4N sites. Using this Tafel slope we postulate that the DV4N site corresponds to those observed in a recently reported, highly active FeNC catalyst, assigned an oxidation state of +3 from XPS studies. The present study provides a rigorous basis for the study of single atom catalysts for CO_2R and beyond, from both the fundamental and catalyst development perspectives.

Methods

Density functional theory calculations were carried out using the Vienna Ab-Initio Software Package (VASP).[44] Implicit solvation and counter charge was added to calculations by using VASPsol.[45] Core electrons were described using Projector Augmented Waves (PAW) potentials.[46] Valence electrons were described by plane waves with kinetic energy up to 500eV. Gaussian smearing with a width of 0.1eV is used. The RPBE[47] functional was used for GGA-DFT calculations, while the HSE06[48,49] functional was used for hybrid calculations. Single-point energies with HSE06 functional on RPBE+U geometries are reported throughout the text. The validity of this approximation is reported in SI Note 4. Hubbard-U corrections were added to the d-orbitals of Iron using the implementation of Dudarev.[23]

Single layer 3x3 graphene was used as a model system.[50] Structures were prepared using the Atomic Simulation Environment.[51] The lattice for undoped graphene was optimized using a 12x12x1 Monkhorst-Pack[52] k-point mesh. The 3x3 single layer graphene structures were made with the obtained lattice parameter. All structures were then treated with 4x4x1 Monkhorst-Pack[52] k-point mesh with at least 16 Å of vacuum. Depending on the vacancy type, carbon atoms in the graphene structure were replaced by Nitrogen and Iron atoms. The structure obtained after creating vacancies and doping was subjected to an optimization of both position and lattice constants (VASP[44] keyword $ISIF = 3$) before adding an adsorbate to the unit cell. All geometries are optimized until forces are less than 0.025

$eV\text{Å}^{-1}$. Transition state geometries and energies were obtained by using the Climbing Image Nudged Elastic Band (CI-NEB)[53] implemented within VASP. Forces on the climbing image were considered as converged if they are lower than 0.05 $eV\text{Å}^{-1}$. The density of states for transition states were obtained by carrying out a single-point with HSE06 at the image associated with the transition state with an 8x8x1 k-point mesh and Gaussian smearing of 0.1eV.

VASPsol[45] places a continuum charge distribution in the vacuum region of the cell with charge density of opposite sign to the excess or deficient charge on the surface. A Debye screening length of 3 Å was chosen as this corresponds to bulk ion concentration of 1 Molar. Similar to recent published work,[29] non-electrostatic parameter TAU was set to zero to avoid numerical instabilities. The continuum charge was varied from 0 to 1e in increments of 0.25e.

The computational hydrogen electrode (CHE)[54] was used to determine reaction energies as a function of potential for reactions with an electron in the reactant or product. The chemical potential of the proton and electron is related to that of H_2 at 0V vs RHE.

$$\mu_{H^+} + \mu_{e^-} = \frac{1}{2}\mu_{H_{2(g)}} \tag{9}$$

Field effects for all adsorbates were included in the model by assuming a linear dependence of binding energies with the surface charge.

$$\Delta E_\sigma = a_0 + a_1\sigma \tag{10}$$

We note that this linear variation of energy with σ is valid only for small additions of electrons in the unit cell. At large surface charges, second order terms would need to be taken into account. However, 4(a,b) both show good fits to lines (R^2 values in the caption), which suggests the 2$^{\text{nd}}$ order terms are negligible.

We calculated the adsorption energies and pDOS for relevant intermediates and transition states of all intermediates as a function of the excess charge, applied by varying the number

of electrons in the simulation cell. The same charging scheme was applied along the entire reaction pathway. We assume that our finite cell size simulations approximate those from an infinitely large cell where both the surface charge density and workfunction approach a constant value along the reaction pathway. This assumption was validated through a convergence test (Figure S16),which shows negligible change in the calculated dipole moment between cell sizes of 4x4 to 5x5. We relate the energetics as a function of charge to those at a function of potential with Equation 2, where we have applied experimental pzcs and capacitances. Reliable estimates of the pzc cannot be obtained for single layer 2D materials with an implicit solvent setup because symmetric unit cells cannot be constructed. Thus, we used an experimental value of the pzc.

The capacitance of pristine graphene 21 $\mu F/cm^2$ [55] and the experimental pzc [56] of -0.07V was used. While the workfunctions of DV4N and DV2N vacancies are different ($\Phi_{DV2N} = 3.95V$ and $\Phi_{DV4N} = 3.74V$), we approximate both vacancies to have the same potential of zero charge. This is because the doping concentrations in experiment are between 2-3% [8] by weight, which would give rise to a negligible shift in pzc from pristine graphene.

Micro-kinetic modelling was carried out using CatMAP, [57] which uses a multiple precision Newton root finding algorithm to determine rates and coverages. Decimal precision of 100, along with a rate convergence tolerance value to 10^{-25} was used. Surface charge density dependence of each state was included to describe the effect of field on each adsorbate.

Experimental binding energies are estimated based on Redhead's [58] analysis of a TPD peak. It is assumed that there is no interaction between CO molecules adsorbed on the surface. This is a reasonable assumption because the iron loading is less that 0.1 mass percent of the catalyst. [18,59] Ref59 also shows that the TPD peak is first order in nature. This is expected for CO desorption, and the rate equation can be written as:

$$\text{rate} = \frac{k_B T}{h} \exp\left(-\frac{G_{TS} - G_{IS}}{k_B T}\right) \tag{11}$$

For this estimate, we assume that $G_{TS} - G_{IS} = E_{FS} - E_{IS}$. This is reasonable because the transition state of CO desorption is final-state like. Further details are provided in the SI.

Acknowledgement

Financial support was provided by V-Sustain: The VILLUM Centre for the Science of Sustainable Fuels and Chemicals (#9455) from VILLUM FONDEN.

Supporting Information Available

Contains coverages from RPBE energetics, CO adsorption energy from experiment, Effect of dispersion correction and relaxation, sensitivity to Hubbard-U, pathway to Methane, continuum charging details, gas phase references, vibrational frequencies and atomic coordinates of CO_2 transition states in xyz format.

References

(1) Nitopi, S.; Bertheussen, E.; Scott, S. B.; Liu, X.; Engstfeld, A. K.; Horch, S.; Seger, B.; Stephens, I. E.; Chan, K.; Hahn, C.; Nørskov, J. K.; Jaramillo, T. F.; Chorkendorff, I. Progress and Perspectives of Electrochemical CO2 Reduction on Copper in Aqueous Electrolyte. *Chem. Rev.* **2019**, *119*, 7610–7672.

(2) Seh, Z. W.; Kibsgaard, J.; Dickens, C. F.; Chorkendorff, I.; Nørskov, J. K.; Jaramillo, T. F. Combining Theory and Experiment in Electrocatalysis: Insights into Materials Design. *Science (80-.).* **2017**, *355*.

(3) Jouny, M.; Luc, W.; Jiao, F. General Techno-Economic Analysis of CO2 Electrolysis Systems. *Ind. Eng. Chem. Res.* **2018**, *57*, 2165–2177.

(4) Chen, Y.; Li, C. W.; Kanan, M. W. Aqueous CO2 Reduction at very Low Overpotential on Oxide-derived Au Nanoparticles. *J. Am. Chem. Soc.* **2012**, *134*, 19969–19972.

(5) Möller, T.; Ju, W.; Bagger, A.; Wang, X.; Luo, F.; Ngo Thanh, T.; Varela, A. S.; Rossmeisl, J.; Strasser, P. Efficient CO 2 to CO Electrolysis on Solid Ni-N-C Catalysts at Industrial Current Densities. *Energy Environ. Sci.* **2019**, *12*, 640–647.

(6) Su, H.; Zhao, X.; Cheng, W.; Zhang, H.; Li, Y.; Zhou, W.; Liu, M.; Liu, Q. Hetero-N-Coordinated Co Single Sites with High Turnover Frequency for Efficient Electrocatalytic Oxygen Evolution in an Acidic Medium. *ACS Energy Lett.* **2019**, *4*, 1816–1822.

(7) Shen, J.; Kolb, M. J.; Göttle, A. J.; Koper, M. T. DFT Study on the Mechanism of the Electrochemical Reduction of CO2 Catalyzed by Cobalt Porphyrins. *J. Phys. Chem. C* **2016**, *120*, 15714–15721.

(8) Gu, J.; Hsu, C. S.; Bai, L.; Chen, H. M.; Hu, X. Atomically Dispersed Fe3+ Sites Catalyze Efficient CO2 Electroreduction to CO. *Science (80-.).* **2019**, *364*, 1091–1094.

(9) Cheng, M. J.; Kwon, Y.; Head-Gordon, M.; Bell, A. T. Tailoring Metal-Porphyrin-Like Active Sites on Graphene to Improve the Efficiency and Selectivity of Electrochemical CO2 Reduction. *J. Phys. Chem. C* **2015**, *119*, 21345–21352.

(10) Ringe, S.; Clark, E. L.; Resasco, J.; Walton, A.; Seger, B.; Bell, A. T.; Chan, K. Understanding Cation Effects in Electrochemical CO2 Reduction. *Energy Environ. Sci.* **2019**, *12*, 3001.

(11) Hong, S.; Rahman, T. S. Rationale for the Higher Reactivity of Interfacial Sites in Methanol Decomposition on Au13/TiO2(110). *J. Am. Chem. Soc.* **2013**, *135*, 7629–7635.

(12) Leung, K.; Rempe, S. B.; Schultz, P. A.; Sproviero, E. M.; Batista, V. S.; Chandross, M. E.; Medforth, C. J. Density functional theory and DFT+U study of transition

metal porphines adsorbed on Au(111) surfaces and effects of applied electric fields. *J. Am. Chem. Soc.* **2006**, *128*, 3659–3668.

(13) Keith, J. A.; Carter, E. A. Theoretical Insights into Pyridinium-based Photoelectrocatalytic Reduction of CO2. *J. Am. Chem. Soc.* **2012**, *134*, 7580–7583.

(14) Gray, C. M.; Saravanan, K.; Wang, G.; Keith, J. A. Quantifying Solvation Energies at Solid/Liquid Interfaces using Continuum Solvation Methods. *Mol. Simul.* **2017**, *43*, 420–427.

(15) Bagger, A.; Ju, W.; Varela, A. S.; Strasser, P.; Rossmeisl, J. Single Site Porphyrine-like Structures Advantages over Metals for Selective Electrochemical CO2 Reduction. *Catal. Today* **2017**, *288*, 74–78.

(16) Ju, W.; Bagger, A.; Wang, X.; Tsai, Y.; Luo, F.; Möller, T.; Wang, H.; Rossmeisl, J.; Varela, A. S.; Strasser, P. Unraveling Mechanistic Reaction Pathways of the Electrochemical CO2 Reduction on Fe-N-C Single-Site Catalysts. *ACS Energy Lett.* **2019**, *4*, 1663–1671.

(17) Zhang, C.; Yang, S.; Wu, J.; Liu, M.; Yazdi, S.; Ren, M.; Sha, J.; Zhong, J.; Nie, K.; Jalilov, A. S.; Li, Z.; Li, H.; Yakobson, B. I.; Wu, Q.; Ringe, E.; Xu, H.; Ajayan, P. M.; Tour, J. M. Electrochemical CO2 Reduction with Atomic Iron-Dispersed on Nitrogen-Doped Graphene. *Adv. Energy Mater.* **2018**, *8*.

(18) Varela, A. S.; Kroschel, M.; Leonard, N. D.; Ju, W.; Steinberg, J.; Bagger, A.; Rossmeisl, J.; Strasser, P. PH Effects on the Selectivity of the Electrocatalytic CO2 Reduction on Graphene-Embedded Fe-N-C Motifs: Bridging Concepts between Molecular Homogeneous and Solid-State Heterogeneous Catalysis. *ACS Energy Lett.* **2018**, *3*, 812–817.

(19) Gauthier, J. A.; Dickens, C. F.; Heenen, H. H.; Vijay, S.; Ringe, S.; Chan, K. Unified

Approach to Implicit and Explicit Solvent Simulations of Electrochemical Reaction Energetics. *J. Chem. Theory Comput.* **2019**, *15*, 6895–6906.

(20) Hou, Z.; Wang, X.; Ikeda, T.; Terakura, K.; Oshima, M.; Kakimoto, M. A.; Miyata, S. Interplay between Nitrogen Dopants and Native Point Defects in Graphene. *Phys. Rev. B - Condens. Matter Mater. Phys.* **2012**, *85*, 165439.

(21) Sahraie, N. R.; Kramm, U. I.; Steinberg, J.; Zhang, Y.; Thomas, A.; Reier, T.; Paraknowitsch, J. P.; Strasser, P. Quantifying the Density and Utilization of Active Sites in Non-precious Metal Oxygen Electroreduction Catalysts. *Nat. Commun.* **2015**, *6*.

(22) Luo, F.; Choi, C. H.; Primbs, M. J.; Ju, W.; Li, S.; Leonard, N. D.; Thomas, A.; Jaouen, F.; Strasser, P. Accurate Evaluation of Active-Site Density (SD) and Turnover Frequency (TOF) of PGM-Free Metal-Nitrogen-Doped Carbon (MNC) Electrocatalysts using CO Cryo Adsorption. *ACS Catal.* **2019**, *9*, 4841–4852.

(23) Dudarev, S.; Botton, G. Electron-energy-loss Spectra and the Structural Stability of Nickel Oxide: An LSDA+U study. *Phys. Rev. B - Condens. Matter Mater. Phys.* **1998**, *57*, 1505–1509.

(24) Patel, A. M.; Ringe, S.; Siahrostami, S.; Bajdich, M.; Nørskov, J. K.; Kulkarni, A. R. Theoretical Approaches to Describing the Oxygen Reduction Reaction Activity of Single-Atom Catalysts. *J. Phys. Chem. C* **2018**, *122*, 29307–29318.

(25) Bukas, V. J.; Kim, H. W.; Sengpiel, R.; Knudsen, K.; Voss, J.; McCloskey, B. D.; Luntz, A. C. Combining Experiment and Theory to Unravel the Mechanism of Two-Electron Oxygen Reduction at a Selective and Active Co-catalyst. *ACS Catal.* **2018**, *8*, 11940–11951.

(26) Kim, H. W.; Bukas, V. J.; Park, H.; Park, S.; Diederichsen, K. M.; Lim, J.; Cho, Y. H.; Kim, J.; Kim, W.; Han, T. H.; Voss, J.; Luntz, A. C.; McCloskey, B. D. Mechanisms

of Two-electron and Four-electron Electrochemical Oxygen Reduction Reactions at Nitrogen-doped reduced Graphene Oxide. *ACS Catal.* **2020**, *10*, 852–863.

(27) Nørskov, J. K.; Studt, F.; Abild-Pedersen, F.; Bligaard, T. *Fundam. Concepts Heterog. Catal.*; Wiley Blackwell, 2014; Vol. 9781118888; pp 1–196.

(28) Gauthier, J. A.; Fields, M.; Bajdich, M.; Chen, L. D.; Sandberg, R. B.; Chan, K.; Nørskov, J. K. Facile Electron Transfer to CO2 during Adsorption at the Metal—Solution Interface. *J. Phys. Chem. C* **2019**, *123*, 29278–29283.

(29) Gauthier, J. A.; Ringe, S.; Dickens, C. F.; Garza, A. J.; Bell, A. T.; Head-Gordon, M.; Nørskov, J. K.; Chan, K. Challenges in Modeling Electrochemical Reaction Energetics with Polarizable Continuum Models. *ACS Catal.* **2019**, *9*, 920–931.

(30) Garza, A. J.; Bell, A. T.; Head-Gordon, M. Mechanism of CO2 Reduction at Copper Surfaces: Pathways to C2 Products. *ACS Catal.* **2018**, *8*, 1490–1499.

(31) Cheng, T.; Fortunelli, A.; Goddard, W. A. Reaction Intermediates during Operando Electrocatalysis Identified from Full Solvent Quantum Mechanics Molecular Dynamics. *Proc. Natl. Acad. Sci. U. S. A.* **2019**, *116*, 7718–7722.

(32) Huang, J.; Hörmann, N.; Oveisi, E.; Loiudice, A.; De Gregorio, G. L.; Andreussi, O.; Marzari, N.; Buonsanti, R. Potential-induced Nanoclustering of Metallic Catalysts during Electrochemical CO2 Reduction. *Nat. Commun.* **2018**, *9*.

(33) Kim, D.; Shi, J.; Liu, Y. Substantial Impact of Charge on Electrochemical Reactions of Two-Dimensional Materials. *J. Am. Chem. Soc.* **2018**, *140*, 9127–9131.

(34) Nie, X.; Luo, W.; Janik, M. J.; Asthagiri, A. Reaction Mechanisms of CO2 Electrochemical Reduction on Cu(1 1 1) Determined with Density Functional Theory. *J. Catal.* **2014**, *312*, 108–122.

(35) Strmcnik, D.; Uchimura, M.; Wang, C.; Subbaraman, R.; Danilovic, N.; Van Der Vliet, D.; Paulikas, A. P.; Stamenkovic, V. R.; Markovic, N. M. Improving the Hydrogen Oxidation Reaction Rate by Promotion of Hydroxyl Adsorption. *Nat. Chem.* **2013**, *5*, 300–306.

(36) Dickens, C. F.; Kirk, C.; Nørskov, J. K. Insights into the Electrochemical Oxygen Evolution Reaction with ab initio Calculations and Microkinetic Modeling: Beyond the Limiting Potential Volcano. *J. Phys. Chem. C* **2019**, *123*, 18960–18977.

(37) Shi, C.; Chan, K.; Yoo, J. S.; Nørskov, J. K. Barriers of Electrochemical CO2 Reduction on Transition Metals. *Org. Process Res. Dev.* **2016**, *20*, 1424–1430.

(38) Ringe, S.; Morales-Guio, C. G.; Chen, L. D.; Fields, M.; Jaramillo, T. F.; Hahn, C.; Chan, K. Double Layer Charging Driven Carbon dioxide Adsorption Limits the Rate of Electrochemical Carbon dioxide Reduction on Gold. *Nat. Commun.* **2020**, *11*.

(39) Leonard, N.; Ju, W.; Sinev, I.; Steinberg, J.; Luo, F.; Varela, A. S.; Roldan Cuenya, B.; Strasser, P. The Chemical Identity, State and Structure of Catalytically Active Centers during the Electrochemical CO2 Reduction on Porous Fe-nitrogen-carbon (Fe-N-C) Materials. *Chem. Sci.* **2018**, *9*, 5064–5073.

(40) Peterson, A. A.; Abild-Pedersen, F.; Studt, F.; Rossmeisl, J.; Nørskov, J. K. How Copper Catalyzes the Electroreduction of Carbon Dioxide into Hydrocarbon Fuels. *Energy Environ. Sci.* **2010**, *3*, 1311–1315.

(41) Studt, F.; Abild-Pedersen, F.; Varley, J. B.; Nørskov, J. K. CO and CO2 Hydrogenation to Methanol Calculated using the BEEF-vdW Functional. *Catal. Letters* **2013**, *143*, 71–73.

(42) Christensen, R.; Hansen, H. A.; Vegge, T. Identifying Systematic DFT Errors in Catalytic Reactions. *Catal. Sci. Technol.* **2015**, *5*, 4946–4949.

(43) Campbell, C. T. The Degree of Rate Control: A Powerful Tool for Catalysis Research. *ACS Catal.* **2017**, *7*, 2770–2779.

(44) Kresse, G.; Furthmüller, J. Efficient Iterative Schemes for ab initio Total-energy Calculations using a Plane-wave Basis Set. *Phys. Rev. B - Condens. Matter Mater. Phys.* **1996**, *54*, 11169–11186.

(45) Mathew, K.; Kolluru, V. S.; Mula, S.; Steinmann, S. N.; Hennig, R. G. Implicit Self-consistent Electrolyte Model in Plane-wave Density-functional Theory. *J. Chem. Phys.* **2019**, *151*.

(46) Joubert, D. From Ultrasoft Pseudopotentials to the Projector Augmented-wave Method. *Phys. Rev. B - Condens. Matter Mater. Phys.* **1999**, *59*, 1758–1775.

(47) Hammer, B.; Hansen, L. B.; Nørskov, J. K. Improved Adsorption Energetics Within Density-functional Theory Using Revised Perdew-Burke-Ernzerhof Functionals. *Phys. Rev. B - Condens. Matter Mater. Phys.* **1999**, *59*, 7413–7421.

(48) Heyd, J.; Scuseria, G. E.; Ernzerhof, M. Erratum: Hybrid functionals based on a screened Coulomb potential. *J. Chem. Phys.* **2006**, *124*, 9901.

(49) Heyd, J.; Scuseria, G. E.; Ernzerhof, M. Hybrid functionals based on a Screened Coulomb Potential. *J. Chem. Phys.* **2003**, *118*, 8207–8215.

(50) Tripkovic, V.; Vanin, M.; Karamad, M.; Björketun, M. E.; Jacobsen, K. W.; Thygesen, K. S.; Rossmeisl, J. Electrochemical CO2 and CO Reduction on Metal-functionalized Porphyrin-like Graphene. *J. Phys. Chem. C* **2013**, *117*, 9187–9195.

(51) Hjorth Larsen, A.; JØrgen Mortensen, J.; Blomqvist, J.; Castelli, I. E.; Christensen, R.; Dułak, M.; Friis, J.; Groves, M. N.; Hammer, B.; Hargus, C.; Hermes, E. D.; Jennings, P. C.; Bjerre Jensen, P.; Kermode, J.; Kitchin, J. R.; Leonhard Kolsbjerg, E.; Kubal, J.; Kaasbjerg, K.; Lysgaard, S.; Bergmann Maronsson, J.; Max-

son, T.; Olsen, T.; Pastewka, L.; Peterson, A.; Rostgaard, C.; SchiØtz, J.; Schütt, O.; Strange, M.; Thygesen, K. S.; Vegge, T.; Vilhelmsen, L.; Walter, M.; Zeng, Z.; Jacobsen, K. W. The Atomic Simulation Environment - A Python Library for Working with Atoms. *J. Phys. Condens. Matter* **2017**, *29*, 30.

(52) Monkhorst, H. J.; Pack, J. D. Special Points for Brillouin-zone Integrations. *Phys. Rev. B* **1976**, *13*, 5188–5192.

(53) Henkelman, G.; Uberuaga, B. P.; Jónsson, H. Climbing Image Nudged Elastic Band Method for Finding Saddle Points and Minimum Energy Paths. *J. Chem. Phys.* **2000**, *113*, 9901–9904.

(54) Nørskov, J. K.; Rossmeisl, J.; Logadottir, A.; Lindqvist, L.; Kitchin, J. R.; Bligaard, T.; Jónsson, H. Origin of the Overpotential for Oxygen Reduction at a Fuel-cell Cathode. *J. Phys. Chem. B* **2004**, *108*, 17886–17892.

(55) Chen, J.; Li, C.; Shi, G. Graphene Materials for Electrochemical Capacitors. *J. Phys. Chem. Lett.* **2013**, *4*, 1244–1253.

(56) Choi, C. H.; Lim, H. K.; Chung, M. W.; Chon, G.; Ranjbar Sahraie, N.; Altin, A.; Sougrati, M. T.; Stievano, L.; Oh, H. S.; Park, E. S.; Luo, F.; Strasser, P.; Dražić, G.; Mayrhofer, K. J.; Kim, H.; Jaouen, F. The Achilles' Heel of Iron-based Catalysts during Oxygen Reduction in an Acidic Medium. *Energy Environ. Sci.* **2018**, *11*, 3176–3182.

(57) Medford, A. J.; Shi, C.; Hoffmann, M. J.; Lausche, A. C.; Fitzgibbon, S. R.; Bligaard, T.; Nørskov, J. K. CatMAP: A Software Package for Descriptor-Based Microkinetic Mapping of Catalytic Trends. *Catal. Letters* **2015**, *145*, 794–807.

(58) de Jong, A. M.; Niemantsverdriet, J. W. Thermal Desorption Analysis: Comparative Test of Ten Commonly Applied Procedures. *Surf. Sci.* **1990**, *233*, 355–365.

(59) Varela, A. S.; Ranjbar Sahraie, N.; Steinberg, J.; Ju, W.; Oh, H. S.; Strasser, P. Metal-Doped Nitrogenated Carbon as an Efficient Catalyst for Direct CO2 Electroreduction to CO and Hydrocarbons. *Angew. Chemie - Int. Ed.* **2015**, *54*, 10758–10762.

Graphical TOC Entry